Modeling of an active torsion bar automotive suspension for ride comfort and energy analysis in standard road profiles

Rafael Tavares * **Joan Vazquez Molina** ** **Monzer Al Sakka** **
Miguel Dhaens ** **Michael Ruderman** *

* *University of Agder, Faculty of Engineering and Science, Grimstad, Norway (email: rafael.tavares@uia.no, michael.ruderman@uia.no)*
** *Tenneco Automotive BVBA, Sint-Truiden, Belgium (e-mail: jvazquezmolina@tenneco.com, msakka@tenneco.com, mdhaens@tenneco.com)*

Abstract:
Chassis technology is evolving towards active suspension, in which actuators can provide forces to each wheel individually. This overcomes the traditional trade-off between comfort and handling, at the expense of increased complexity and electric consumption. To reduce power demand, regenerative solutions capable of harvesting a certain amount of energy otherwise dissipated in vehicle suspensions and to enhance vehicle dynamics for improving ride comfort and road safety at the same time have been researched. In this paper, an active suspension based on a torsion bar is modeled and analyzed under the excitation from standardized road profiles according to the ISO 8608 norm. A skyhook controller was implemented in a quarter-car model for assessment of the ride comfort, power consumption and harvesting potential of a DC motor according to the four-quadrant operation, working as a generator. From simulations, results show that for a velocity of 50 km/h it is possible to harvest 50-60 W from a vehicle driving in a class C road with ride comfort trade-off. This constitutes around 25% of the power consumption of the active suspension system.

Keywords: Modeling, Mechatronic systems, Vehicle dynamic systems, Motion control, Energy harvesting, Regenerative suspension, Ride comfort, Road profiles

1. INTRODUCTION

Chassis technology for high-end cars is evolving towards electromechanical active suspensions in which actuators provide forces to each wheel individually. In quarter car models, active control shows significant improvement in ride performance, both in terms of handling (tire deflection) and comfort (chassis acceleration, suspension deflection, harshness) simultaneously (see Rajamani (2012)). This overcomes the traditional trade-off between comfort and handling, at the expense of increased complexity and electric consumption. Harvesting the energy otherwise dissipated by the shock absorbers is potentially advantageous, since reducing power consumption is necessary to improve fuel economy, reduce emissions, and supply the power demand of additional systems (see Zuo and Tang (2013)). Moreover, although active suspension and harvesting are independent, the current automotive electrification trend supports the integration of these technologies into future chassis designs, making it even more relevant when considering the importance of driving range in electric cars.

Active suspension systems based on anti-roll bar techniques, such as the Delft Active Suspension (Venhovens and van der Knaap (1995)) and the BMW Active Drive (Strassberger and Guldner (2004)), have been effectively used to implement self-leveling features and to improve ride comfort in passenger vehicles. In this work, we focus on modeling and analyzing an alternative configuration where the mechanism is aligned with the axles of the vehicle, providing a more compact solution with a higher force actuation range. For other approaches and a state-of-the-art review on active suspensions, we refer to Tseng and Hrovat (2015) and references within.

In this paper, the active torsion bar (ATB) system is modelled with the intent of estimating the potential harvesting power, for better comparison with other intelligent suspension systems. This mechanism has recently been proposed in several patents, e.g. Ovalo GmbH (2017) and Schmitt (2017), and consists of an torsion bar which can be pretensioned with an external torque powered by an electric motor. This system is capable of transmitting a force into each wheel individually, providing the role of an active anti-roll bar, and can switch between active and recuperation mode. The electrical motor can work reversely as a generator, thus reducing the systems' energy consumption. For examples of the use of permanent magnet DC motors in regenerative dampers for vehicle suspension applications see Liu et al. (2011) and references therein. For passenger vehicles, the potential harvesting

This research receives funding from the European Community Horizon 2020 Research and Innovation Programme (H2020-MSCA-RISE-2016) under the Marie Skłodowska-Curie grant agreement No 734832.

goes up to 100-400 W per vehicle, which translates into 2-3% fuel efficiency, depending on road conditions and vehicle speed as referred in Abdelkareem et al. (2018) and Zuo and Zhang (2013). The structure of this paper is as follows. In section II, the electromechanical model of the ATB suspension system is modeled, as well as the standardized road inputs, and in section III the parameters for the model are determined. Section IV describes the implemented control methodologies, and the ride comfort and energy performances of the system are further analyzed in section V. Finally, conclusions are presented in section VI.

2. MODELING OF THE SUSPENSION SYSTEM

The system, shown in Fig. 1, comprises a torsion spring composed by two elements, a hollow torsion (ht) tube and a titanium torsion bar (tb), placed on each vehicle side which are oriented transversely to the vehicle longitudinal center and act on each wheel suspension strut. The two spring element configuration is adopted due to space restrictions, with a transverse central solid bar and an outer tubular bar combined to obtain the required spring characteristics as stated in Schmitt (2017).

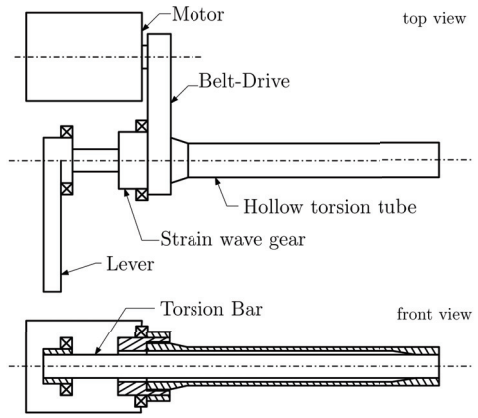

Fig. 1. Structure of the ATB suspension system (adapted from Schmitt (2017)).

The torsion spring is actuated by an electric motor, providing the variable pretension to be transfered to the suspension strut via the output lever. Additionally, the torsion spring bars on both vehicle sides can be coupled by one additional torsion spring element to provide anti-roll. The electric motor torque is transmitted to the hollow torsion tube through a belt and pulley drive transmission and a strain wave transmission gear. The subsystems in the model approach for the ATB system in a quarter-car model under road input excitation are shown in Fig. 2.

The quarter-car model aims to describe the interactions between the suspension system, the tire, and the chassis in a single corner of a vehicle, as shown in Fig. 3. Each corner can be modeled as a two degrees of freedom system to study the response of the vehicle to a profile induced excitation. The modeled ATB system is introduced in the quarter-car model as an actuator placed between the wheel (unsprung mass) and the chassis (suspended mass), in parallel with the spring and damper that constitute the conventional passive suspension.

Applying Newton's second law, the dynamic equations can be written as

$$m_1\ddot{x}_1 = k_1(u - x_1) + b_1(\dot{u} - \dot{x}_1) - k_2(x_1 - x_2) - b_2(\dot{x}_1 - \dot{x}_2) - F_a \quad (1)$$

$$m_2\ddot{x}_2 = k_2(x_1 - x_2) + b_2(\dot{x}_1 - \dot{x}_2) + F_a, \quad (2)$$

assuming 1/4 of the chassis mass m_1, the unsprung mass m_2, the tire stiffness k_1, the tire damping b_1, the spring stiffness k_2, the suspension damping b_2, the wheel displacement x_1, the chassis displacement x_2, the road disturbance u, and the force applied by the ATB system F_a.

The mechanism of the ATB is modeled as the angular two degrees of freedom system shown in Fig. 4, comprising the inertia of the hollow tube J_1 and the inertia of the lever J_2 that are connected by the torsional spring comprising the stiffness of the two elements: the hollow tube and the torsion bar. This system is fixed to the chassis and is capable of transmitting the force F_a through a coupling rod that is placed between the lever and the suspension strut. The angular motion equations can be written as

$$J_1\ddot{\theta}_1 = T_{tr} - K_{eq}(\theta_1 - \theta_2) \quad (3)$$

$$J_2\ddot{\theta}_2 = T_f + K_{eq}(\theta_1 - \theta_2), \quad (4)$$

where T_{tr} is the external torque from the gearbox transmission and T_f is the torque transmitted to the lever. The equivalent torsional spring coefficient is given by

$$K_{eq} = \left(\frac{1}{K_{ht}} + \frac{1}{K_{tb}}\right)^{-1}. \quad (5)$$

The geometric relation between the position of the lever θ_2 and the suspension travel $x_1 - x_2$, shown in Fig. 4 (b), is given by the trigonometric relationship

$$x_1 - x_2 = l\sin(\theta_2), \quad (6)$$

where l is the lever's length, and the torque-force relationship is given by

$$T_f = Fl\cos(\theta_2). \quad (7)$$

Note that if there is no external torque from the transmission, this constitutes a torsion spring in parallel with the translational spring k_2 and the damper b_2.

The motor torque is transmitted to one end of the torsion spring hollow tube by a two-stage transmission constituted by a belt-drive and a gearbox. The output torque T_o is then given by

$$T_o = T_i r, \quad (8)$$

where T_i and r are the input torque and the transmission ratio, respectively. The transmission ratio can also be used to write the relationship between input and output angular velocity ω_o

$$\omega_o = \dot{\theta}_o = \frac{\dot{\theta}_i}{r}. \quad (9)$$

Considering the mechanical power $P = T\omega$, the losses on both transmissions can be considered by introducing the efficiency factor η,

$$T_o\dot{\theta}_o = \eta T_i\dot{\theta}_i. \quad (10)$$

We declare the indexes $i \in \{m, p, tr\}$ for input and $o \in \{m, p, tr\}$ for output. Then, equations (8) and (9) establish the relationship between the torques and angular velocities, with according input and outputs for each subsystem as shown in Fig. 2.

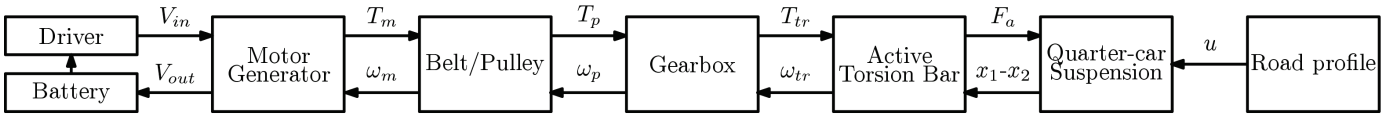

Fig. 2. Model of active torsion spring bar suspension

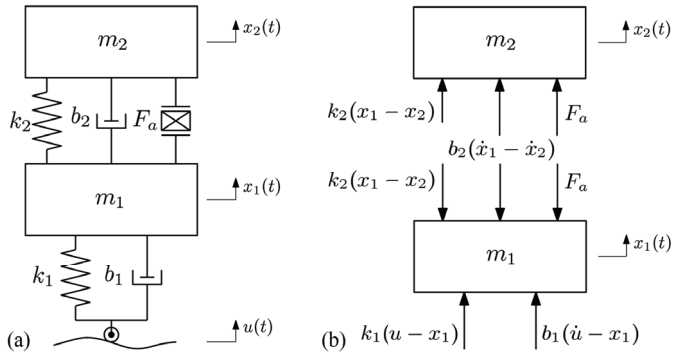

Fig. 3. Quarter-car (a) suspension model and (b) free-body diagram.

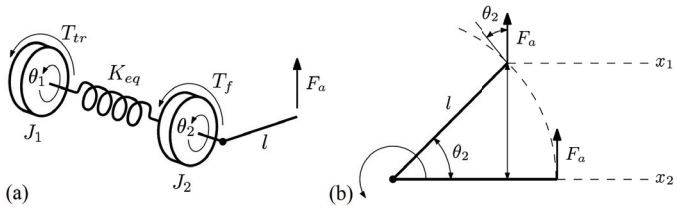

Fig. 4. Torsion bar model: (a) Mechanical arrangement and (b) Geometric relation between θ_2 and $x_1 - x_2$.

A DC motor provides the variable pre-tension of the torsion spring system, and can be in reserve operated as a generator to convert mechanical movement of the shaft due to suspension travel into electrical energy. The electric equivalent circuit of the armature and the free-body diagram of the rotor are shown in Fig. 5. For simplification, we are considering one winding instead of the delta three windings typical in brushless DC motors.

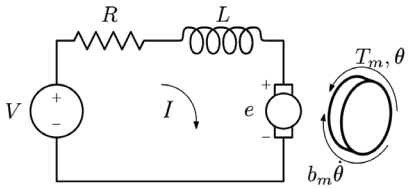

Fig. 5. Armature circuit and rotor equivalent for a DC motor.

In general, the torque generated by a DC motor is proportional to the armature current and the strength of the magnetic field. Assuming that the magnetic field distribution is homogeneous, the motor torque is given by

$$T_m = IK_t, \tag{11}$$

where I is the armature current and K_t is the motor torque constant. The back electromotive force e is proportional to the angular velocity of the motor shaft θ

$$e = K_e\dot{\theta}, \tag{12}$$

being K_e the electromotive force constant. From Newton's second law and Kirchoff's law for the armature circuit, we obtain the governing equations for the DC motor

$$J_m\ddot{\theta} + b_m\dot{\theta} = K_tI \tag{13}$$

$$L\frac{dI}{dt} + RI = V - e, \tag{14}$$

where b_m R, L, V are the motor viscous friction constant, the armature electric resistance, the armature electric inductance and the voltage source/generated (V_{in} or V_{out}), respectively.

2.1 Road profile generation

The standard ISO 8608 specifies the road classification of longitudinal road profiles based on vertical displacement power spectral density (PSD). For an extensive comparison of the parameters used to simulate road profiles based on the ISO 8608 we refer to Múčka (2017) and references therein. The road roughness is typically represented as a stationary Gaussian stochastic process of a given displacement PSD in $\mathrm{m}^2/(\mathrm{cycle/m})$

$$S_{\mathrm{PSD}}(\nu) = G_r\nu^{\beta}, \tag{15}$$

where ν is the spatial frequency (cycle/m), $G_r = S_0/\nu_0^{\beta}$ is the road roughness coefficient, S_0 is the displacement PSD at the reference spatial frequency $\nu_0 = 1/2\pi$, and the β fitting parameter commonly approximated as -2. The ISO classification is based on the value of S_0 as shown in Table 1 (adapted from Zuo and Zhang (2013)).

Table 1. Road roughness S_0 $[\mathrm{m}^2/(\mathrm{cycle/m})]$ according to ISO 8608 classification

Road class	S_0 **range,** $\times 10^{-6}$	S_0 **mean,** $\times 10^{-6}$
A (Very good)	< 8	4
B (Good)	$8 - 32$	16
C (Average)	$32 - 128$	64
D (Poor)	$128 - 512$	256
E (Very poor)	$512 - 2048$	1024
F	$2048 - 8192$	4096
G	$8192 - 32768$	16384
H	> 32768	

Accurate road profiles based on the ISO 8608 can be modeled as white noise input through a first order filter Zuo and Zhang (2013). Considering $\omega = 2\pi v\nu$, the PSD of the road profile can be expressed as

$$S_{\mathrm{PSD}}(\omega) = \frac{2\pi G_r v}{\omega^2 + \omega_0^2}, \tag{16}$$

where v is the vehicle velocity and ω_0 is the cutoff frequency to remove small spectral frequencies. The road disturbance can then be modeled as a white noise signal filtered by a first-order filter defined as

$$G(s) = \frac{\sqrt{2\pi G_r v}}{s + \omega_0}. \tag{17}$$

Examples of road profiles generated through the described method for $v = 50$ km/h are shown in Fig. 6.

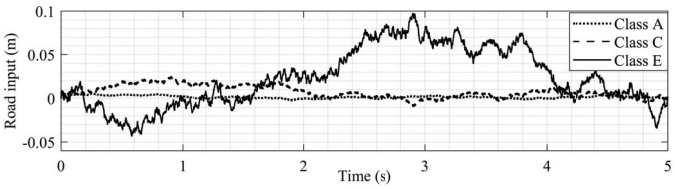

Fig. 6. Road profiles according to the ISO 8608 standard.

3. MODEL PARAMETERS

The model parameters were determined based on the technical information from Köbler and Schmitt (2019), Adcock (2019), Jablonowski et al. (2017), Willems (2012) and Schmitt (2017). The 2 kW electric motors at each corner are connected by a mechanical belt and pulley with a transmission ratio of 1:2.36 to an Ovalo Strain Wave Gear, that delivers a high transmission ratio of 1:80 transmitted through a torsion shaft and bar to a link into the steering knuckle. The electric motor is powered by the 48 V main electrical system. The ATB system adds a total weight of 65 kg per axle, considering a D to E-segment sized passenger vehicle (according to EEC (1999)).

The titanium torsion bar has a length of $l_{tb} = 0.4$ m and a diameter of $d_{tb} = 22$ mm, according to Köbler and Schmitt (2019). The maximum angle of the level when the torsion spring is pre-tensioned is 20°. The lever can exert up to 1100 Nm on the suspension via a coupling rod, which corresponds to a force of 5.0 kN (front) or 4.5 kN (rear). The control frequency range of the system is 0-6 Hz (Jablonowski et al. (2017)). Available specifications were used to calculate the model parameters. The remaining unknown geometry and dimensions have been assumed according to the patent diagrams. Due to the damper travel limitations, the suspension travel $x_1 - x_2$ was limited to 70 mm, usual value for a car with this weight.

The inertia polar moment at the centroid p is given by

$$M_p = \iint_A r^2 dA, \tag{18}$$

and the inertia polar moment at a rotation point o is

$$M_o = M_p + Ad^2, \tag{19}$$

considering A the section area and d the distance between the rotation point and the section centroid. Assuming the simplified geometry sections, the inertia polar moment for the torsion bar, hollow tube and lever can be calculated from their approximate geometries by

$$M_p = \frac{\pi}{32} d_{tb}^4 \tag{20}$$

$$M_p = \frac{\pi}{32} \left(d_{ht}^4 - d_{tb}^4\right) \tag{21}$$

$$M_p = \frac{\pi}{32} d_{ht}^4 + \frac{\pi}{8} d_{ht}^2 l_l^2 + \frac{1}{12} \left(d_{ht}^3 + l_l^3\right) + \frac{l_l^3 d_{ht}}{4}. \tag{22}$$

The polar mass inertia J_p is given by

$$J_p = M_p \rho h \tag{23}$$

where ρ is the material volumetric mass density and h the length of the section.

The torsional spring coefficient K can be calculated from

$$K = \frac{T_f}{\theta} = \frac{GM_p}{l}, \tag{24}$$

where G is the material modulus of rigidity. All model parameters are listed in Table 2.

Table 2. Model parameters

Parameter		Value	Units
R	Armature resistance	1	Ω
L	Armature inductance	0.1	H
K_t	Torque constant	0.13	Nm/A
K_e	Electromotive force constant	0.2	Vs/rad
b_m	Viscious friction constant	0.25	Ns/m
J_m	Rotor moment of inertia	0.01	kg m^2
m_1	Unsprung mass	50	kg
m_2	Sprung mass	516.25	kg
k_1	Tire elastic coefficient	300000	N/m
k_2	Passive spring coefficient	70000	N/m
b_1	Tire damping coefficient	1400	Ns/m
b_2	Passive damping coefficient	8000	Ns/m
r_b	Belt drive transmission ratio	2.36	-
r_{gb}	Gearbox transmission ratio	80	-
η_b	Belt drive efficiency	95	%
η_{gb}	Gearbox efficiency	95	%
d_{ht}	Hollow tube diameter	0.030	m
d_{tb}	Torsion bar diameter	0.022	m
l_{ht}	Hollow tube length	0.240	m
l_{tb}	Torsion bar length	0.400	m
l_l	Lever length	0.200	m
G_s	Steel modulus of rigidity	210	GPa
G_t	Titanium modulus of rigidity	105	GPa
ρ_s	Steel density	7.85x10^3	kg/m^3
ρ_t	Titanium density	4.51x10^3	kg/m^3
Polar moments of inertia			
$M_{p,tb}$	Torsion bar	2.3x10^{-8}	m^4
$M_{p,ht}$	Hollow tube	5.65x10^{-8}	m^4
$M_{p,lvr}$	Lever	7.43x10^{-4}	m^4
Mass moments of inertia			
$J_{p,tb}$	Torsion bar	4.149x10^{-5}	kg m^2
$J_{p,ht}$	Hollow tube	1.065x10^{-4}	kg m^2
$J_{p,lvr}$	Lever	0.167	kg m^2
Torsional elastic constants			
K_{tb}	Torsion bar	1.089x10^7	kg m^2/s^2
K_{ht}	Hollow tube	4.659x10^7	kg m^2/s^2
K_{eq}	Equivalent	8.827x10^6	kg m^2/s^2

4. CONTROL ARCHITECTURE

4.1 Motor torque control

A PID controller loop was implemented for the motor torque. The K_p, K_i and K_d controller parameters were adjusted considering that a minimal overshoot in the voltage input is allowed and the settling time was based on the response frequency of the system. The comparison between the open- and closed-loop response of the controlled motor torque are shown in Fig. 7, the controller gains were set to $K_p = 1.677$, $K_i = 37.36$ and $K_d = 0.024$. The transient peak on the control voltage above the rated value is compliant with the maximum power admitted for short-term operation out of the rated values (typically 10% of the duty cycle (Bosch (2013))).

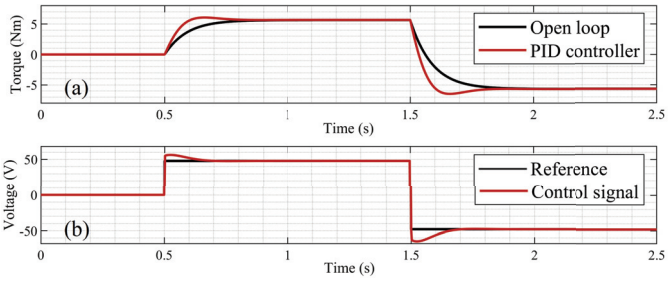

Fig. 7. Open- and closed-loop response of the controlled motor torque: (a) Output torque; (b) Control voltage.

4.2 Skyhook control

Skyhook control is a comfort-oriented control strategy introduced by Karnopp et al. (1974). The principle of this approach is to design an active suspension control that mimics a chassis that is virtually connected to the sky to reduce its vertical oscillations, as shown in Fig. 8. This is achieved by a virtual damper connecting the sprung mass to a stationary reference, which isolates the sprung mass from the road profile. The damper force is given by

$$F_{\text{sky}} = b_{\text{sky}}\dot{x}_2. \tag{25}$$

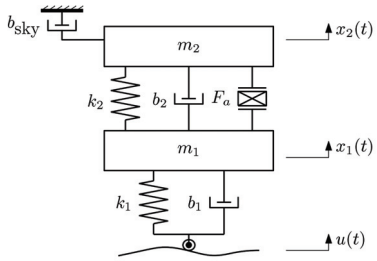

Fig. 8. Quarter-car model with skyhook control.

Figure 9 shows the comparison of the chassis displacement x_2 of the quarter-car model in passive mode and with skyhook control, considering the nominal chassis mass m_2.

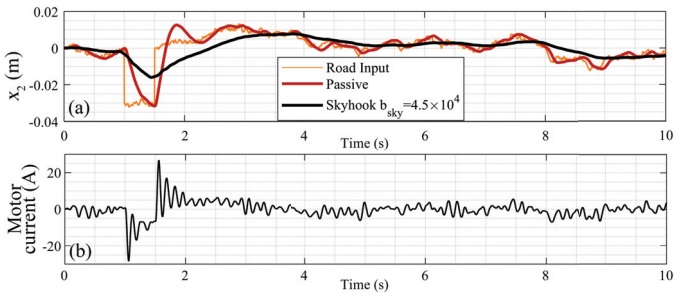

Fig. 9. Comparison of (a) x_2 in passive mode and skyhook control, and (b) Motor current (nominal m_2)

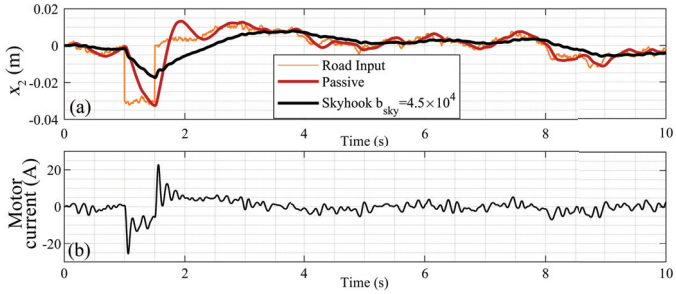

Fig. 10. Comparison of (a) x_2 in passive mode and skyhook control, and (b) Motor current (disturbance in m_2)

The system was then evaluated under a disturbance on m_2. We consider a realistic condition of a full loaded car, represented by an increase of m_2 by 25%. All remaining system and control parameters were unchanged. Figure 10 shows the comparison of the chassis displacement x_2 of the quarter-car model in passive mode and with skyhook control, considering additional 25% of mass m_2. A small increase in the chassis displacement x_2 can be observed in the passive mode, as well as the robustness of skyhook controller to realistic uncertainties in the sprung mass m_2.

4.3 Four-quadrant operation for energy harvesting

The steady-state speed of the DC motor is determined by the applied voltage in the armature, and the motor torque is directly proportional to the armature current as established in eq. (11). The DC motor can develop positive (motoring) or negative (generating) torque by controlling the extent to which the applied voltage is greater or less than the back electromotive force. This operation is known as regenerative braking of DC motors in four-quadrant operation (Krishnan (2009) and Hughes and Drury (2013)), shown in Fig. 11. Most of the input mechanical power is converted to electrical power, being the rest lost as heat in the armature circuit. During the deceleration, kinetic energy from the motor and load inertias can be returned to the supply. This effect is therefore an example of regenerative braking, which occurs in the II and IV quadrants, when $T_m\omega_m<0$, stating the condition for harvesting energy from the road vibration.

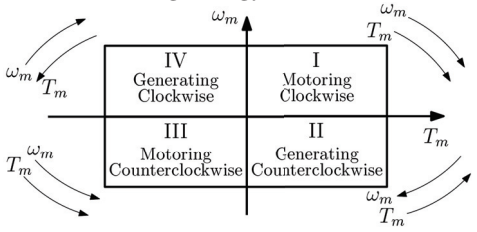

Fig. 11. Four-quadrant operation mode of DC motors.

5. RESULTS AND DISCUSSION

In the automotive industry, ride comfort is often referred as the capability of damping and isolation of road vibrations in three main frequency range intervals: 0-3 Hz (primary ride), 3-8 Hz (choppiness) and 8-100 Hz (shake and road filtering). Fig. 12 shows the response of the quarter-car model with ATB system for different skyhook gains, where it is seen that $b_{sky} = 4.5 \times 10^4$ provides the best damping for the 0-3 Hz without losing damping properties for >8 Hz ranges. Passive suspension is shown as reference.

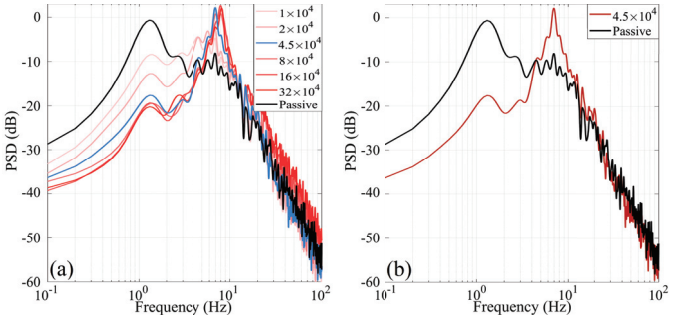

Fig. 12. Skyhook (a) gain sweep and (b) $b_{sky} = 4.5 \times 10^4$.

Figure 12 b) shows that when using the determined skyhook gain, an amplification effect in the 3-8 Hz frequency range is observed. This effect can be minimized by lowering the passive damping coefficient b_2 as shown in Fig. 13 a).

Car manufacturers using this system claim a power consumption around 40-60 W in a city environment, 10-20 W on highways, and up to 250 W on rough roads, see Adcock (2018). Motor power consumption is given by

$$P = VI. \tag{26}$$

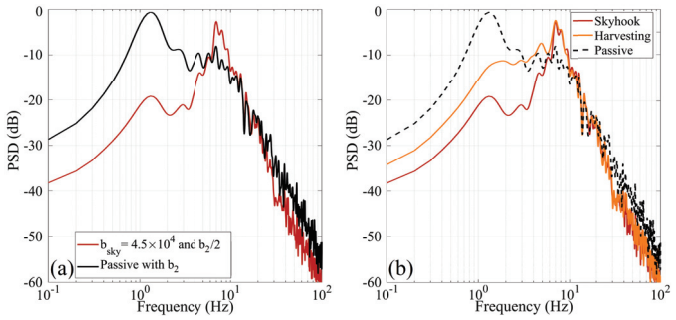

Fig. 13. Comparison between passive mode and: (a) Skyhook with lower passive damping; (b) Harvesting mode when $T_m\omega_m < 0$.

The average and peak power consumptions of a quarter-car model with skyhook control for the different standardized road inputs are shown in Table 3, with values computed for 60 seconds road simulations considering $v = 50$ km/h.

Table 3. Energy consumption in active mode

Road class	Average Power	Peak Power
A (Very good)	4.80 W	65.85 W
B (Good)	19.18 W	263.3 W
C (Average)	76.62 W	1051.2 W
D (Poor)	297.93 W	1980.2 W
E (Very poor)	793.44 W	2121.6 W

Energy harvesting due to regenerative breaking of DC motor according to the four-quadrant operation mode and the trade-off between ride comfort and harvesting/power consumption is shown in Fig.13 b). The average consumed power when in I and III quadrants, and the harvested power when in II and IV quadrants are shown in Table 4, calculated for same conditions as previously. Note that the harvested power represents from 20 to 30% of the consumed power, and this relation increases with the road quality deterioration.

Table 4. Energy balance in harvesting mode

Road class	Consumed Power	Harvested Power
A (Very good)	3.9 W	0.9 W
B (Good)	15.5 W	3.6 W
C (Average)	61.8 W	14.9 W
D (Poor)	239.8 W	58.1 W
E (Very poor)	614.8 W	178.6 W

6. CONCLUSIONS

In this paper, a model for the ATB system was implemented for assessing ride comfort, power consumption and potential energy harvesting under road irregularities generated according to the ISO standard.

With the inclusion of the ATB system in quarter-car suspension, it is possible to improve overall response over the relevant frequency range (0-100 Hz) with optimization of the skyhook control gain and with a lower passive damping coefficient than a conventional suspension system.

The power consumption of the system under skyhook control strategies can be reduced by taking advantage of the generating quadrants of the four-quadrant operation mode in DC motors. Simulations show that for a velocity of 50 km/h it is possible to harvest 50-60 W from the shock absorbers in a class C road with ride comfort trade-off. This constitutes around 25% of the power consumption of the ATB system when working in active suspension mode.

REFERENCES

Abdelkareem, M.A.A., Xu, L., Ali, M.K.A., Elagouz, A., Mi, J., Guo, S., Liu, Y., and Zuo, L. (2018). Vibration energy harvesting in automotive suspension system: A detailed review. *Applied Energy*, 229(C), 672–699.

Adcock, I. (2019). Audi details new A8 active suspension. URL `https://www.sae.org/news/2017/07/audi-details-new-a8-active-suspension/`.

Bosch (2013). Bosch Electric Motors. *Automotive Aftermarket Catalogue (1 987 721 540/201210)*.

EEC (1999). EC Regulation No 4064/89 Merger Procedure. *Europäische Komission, Brüssel*.

Hughes, A. and Drury, W. (2013). *Electric motors and drives: fundamentals, types and applications*. Elsevier.

Jablonowski, C., Schimmel, C., and Underberg, V. (2017). The chassis of the all-new Audi A8. In *8th International Munich Chassis Symposium 2017*, 7–26. Springer.

Karnopp, D., Crosby, M.J., and Harwood, R. (1974). Vibration control using semi-active force generators. *Journal of engineering for industry*, 96(2), 619–626.

Köbler, J. and Schmitt, J. (2019). Superior ride - the audi A8 active suspension. URL `https://audi-dialoge.de/en/aktivfahrwerk/`.

Krishnan, R. (2009). *Permanent magnet synchronous and brushless DC motor drives*. CRC press.

Liu, S., Wei, H., and Wang, W. (2011). Investigation on some key issues of regenerative damper with rotary motor for automobile suspension. In *Proceedings of IEEE 2011 Int. Conf. on Electronic & Mechanical Engineering and Information Technology (EMEIT)*, 1435–1439.

Múčka, P. (2017). Simulated road profiles according to ISO 8608 in vibration analysis. *Journal of Testing and Evaluation*, 46(1), 1–14.

Ovalo GmbH (2017). Active suspension. European Patent Application EP3409516A1.

Rajamani, R. (2012). *Vehicle Dynamics and Control, 2ed*. Springer.

Schmitt, J. (2017). Torsion spring bar system for a wheel suspension of a motor vehicle. US Patent 9,694,645.

Strassberger, M. and Guldner, J. (2004). BMW's dynamic drive: an active stabilizer bar system. *IEEE Control Systems Magazine*, 24(4), 28–29.

Tseng, H.E. and Hrovat, D. (2015). State of the art survey: active and semi-active suspension control. *Vehicle system dynamics*, 53(7), 1034–1062.

Venhovens, P.T. and van der Knaap, A. (1995). Delft active suspension (DAS). background theory and physical realization. *Smart vehicles*.

Willems, M. (2012). Chances and concepts for recuperating damper systems. In *21st Aachen Colloquium Automobile and Engine Technology, Germany*, 765–784.

Zuo, L. and Tang, X. (2013). Large-scale vibration energy harvesting. *Journal of intelligent material systems and structures*, 24(11), 1405–1430.

Zuo, L. and Zhang, P.S. (2013). Energy harvesting, ride comfort, and road handling of regenerative vehicle suspensions. *Journal of Vibration and Acoustics*, 135(1), 011002.